Reachable Dynamics of Networked Microgrids With Large Disturbances

Yifan Zhou, *Member, IEEE*, Peng Zhang, *Senior Member, IEEE*, and Meng Yue, *Member, IEEE*

***Abstract*—An ordinary-differential-equation (ODE) enabled reachable dynamics analysis approach is devised to provably enclose all possible dynamic trajectories of networked microgrids (NMs) under both uncertain renewable power injections and intermittent large disturbance events. As a formal verification tool for the NM dynamics, its new contributions are threefold: 1) An ODE-enabled NMs model is established with a thorough formulation of the hierarchical control of DERs as well as the network transients; 2) A hybrid automaton method is established to empower the reachability analysis of dynamic transitions in NMs caused by arbitrary large disturbances; 3) A zonotope bundle technique is introduced in the reachable set calculation to capture the fast transients and strong nonlinearity upon the occurrence of disturbances, which allows for the reliable formal verification with superior precision and convergence performance. Extensive case studies are performed to demonstrate the effectiveness of the new approach in formally verifying the dynamical performance of disturbed NMs equipped with hierarchical inverter control.**

***Index Terms*—Networked microgrids, reachability analysis, large disturbance, hierarchical control, zonotope bundle.**

I. Introduction

NETWORKED microgrids (NMs) are envisioned to be potent solutions to enhance electricity resiliency for communities and utilities and to host distributed energy resources (DERs) [1]–[3]. Today's low-inertia NM system [4], however, is highly susceptible to transient processes [5] initiated by the highly uncertain DERs, plug-and-play operations and unforeseeable faults [6], [7]. Hence, verifying the dynamic performance becomes a prominent issue in NMs study [8].

NMs are prone to both large disturbances such as faults/contingencies (in brief, 'disturbance') and small but long-lasting perturbations caused by DER uncertainties (in brief, 'perturbation'). Unfortunately, neither the existing direct methods nor time-domain simulation methods [9] can effectively address the impact of those uncertainties on NMs [10]. Even though various approximated Lyapunov functions are introduced [11]–[13], it is still intractable to construct Lyapunov functions [14] for complex NMs and to perform guaranteed conservative stability assessment under various uncertainties. Probabilistic time-domain simulations such as Monte Carlo sampling are prohibitively expensive in considering uncertainties from DERs and random contingencies [15]–[17]. Furthermore, all those methods fail to verify the virtually infinite scenarios and inevitably lead to overly optimistic evaluations.

Recently, reachability analysis is introduced to verify the NMs dynamics [18], [19], where reachable sets are computed to bound all dynamic trajectories under uncertainty perturbations. The prior studies in [18], [19] only consider small-signal perturbations and rely on a quasi-static assumption which neglects network dynamics. Consequently, those methods cannot handle large disturbance events which are of critical importance for verifying the NMs performance. Moreover, the DAE- and zonotope-based algorithms in [18], [19] suffer from the accumulated errors due to the interactions between the algebraic and differential equations and the overly conservative set computations, which plagues their capabilities in handling fast dynamics under large disturbances.

Motivated by the existing challenges, this paper devises an ODE-enabled NMs transient verification methodology enhanced by hybrid automaton to provably enclose all possible dynamic trajectories triggered by arbitrary perturbations and large disturbances. To improve the numerical stability of reachability analysis for the fast dynamics, a zonotope bundle technique is further introduced in the NMs formal verification. The novelties of this work are threefold:

- An ODE-enabled formulation incorporating droop and secondary controls for DERs and the network transients is established for numerically accurate and stable reachability analysis of NMs.
- A generalized NM dynamics verification method is devised by integrating the hybrid automaton and transition functions with reachability analysis. The hybrid reachability approach is able to cope with arbitrary large disturbances overlaid with uncertainties.
- A zonotope bundle technique is implemented to enable accurate and robust NM dynamics verification in the presence of large disturbances and fast dynamics.

The remainder of the paper is organized as follows. Section II establishes the ODE-enabled NMs model with hierarchical control of DERs. Section III devises the NMs dynamic verification. Section IV offers case studies on a typical NM system to validate

Manuscript received May 3, 2020; revised August 20, 2020 and September 28, 2020; accepted October 25, 2020. Date of publication October 30, 2020; date of current version April 19, 2021. This work was supported in part by the Department of Energy's Advanced Grid Modeling Program and in part by the National Science Foundation under Grant ECCS-1831811. Paper no. TPWRS-00727-2020. *(Corresponding author: Peng Zhang.)*

Yifan Zhou and Peng Zhang are with the Department of Electrical and Computer Engineering, Stony Brook University, Stony Brook, NY 11794 USA (e-mail: yifan.zhou.1@stonybrook.edu; p.zhang@stonybrook.edu).

Meng Yue is with the Brookhaven National Laboratory, Upton, NY 11973-5000 USA (e-mail: yuemeng@bnl.gov).

Color versions of one or more of the figures in this article are available online at https://ieeexplore.ieee.org.

Digital Object Identifier 10.1109/TPWRS.2020.3034886

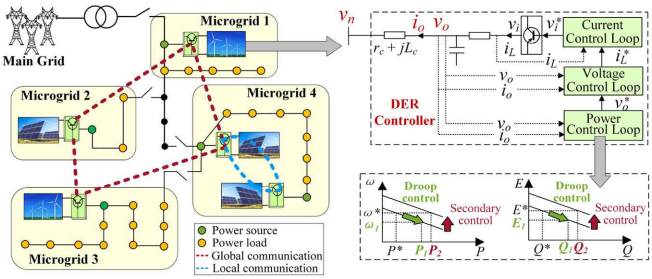

Fig. 1. Schematic NMs with hierarchical control.

the new method, followed by Section V which concludes the paper.

II. ODE-Enabled NMs Dynamics Model

This Section establishes an ODE-enabled dynamic formulation for the NMs with hierarchical Control. Fig. 1 illustrates the schematic of a typical NM system.

A. Formulation of NMs With Hierarchical Control

Without loss of generality, a two-layer hierarchical control is considered in NMs. Locally, the droop control enables the DER's inverter to mimic the frequency and voltage regulation mechanisms of a traditional synchronous generator. Globally, the leader DER in each microgrid communicates with the neighboring microgrids to perform the secondary control which achieves power sharing and restores voltages and frequency in NMs, while the follower DERs in each microgrid assist their leader DER to achieve the global control objectives (see Fig. 1).

The droop control of each DER is formulated as:

$$\boldsymbol{\omega} = \omega^* - \boldsymbol{m}_p(\boldsymbol{P} - (\boldsymbol{P}^* + \boldsymbol{u})) + \boldsymbol{\Omega} \tag{1a}$$

$$\boldsymbol{E} = \boldsymbol{E}^* - \boldsymbol{n}_q(\boldsymbol{Q} - \boldsymbol{Q}^*) + \boldsymbol{e} \tag{1b}$$

where $\boldsymbol{\omega}$ denotes the vector of the DERs' angular speeds; $\boldsymbol{E}$ denotes the vector of output voltage magnitudes; $\boldsymbol{P}$ and $\boldsymbol{Q}$ respectively denote the active/reactive power output of DERs; ω^*, $\boldsymbol{E}^*$, $\boldsymbol{P}^*$ and $\boldsymbol{Q}^*$ respectively denote the nominal values of each control signal; $\boldsymbol{m}_p$ and $\boldsymbol{n}_p$ respectively denotes the active/reactive power droop gains of DERs; $\boldsymbol{u}$ represents the uncertainty impact of the DER's active power generation; $\boldsymbol{\Omega}$ and $\boldsymbol{e}$ denote the secondary control signals following the distributed-averaging proportional-integral logic [20].

Within each microgrid, the follower DERs perform power sharing as follows:

$$\frac{\mathrm{d}\boldsymbol{\Omega}_f}{\mathrm{d}t} = -\boldsymbol{\alpha}_f(\boldsymbol{\omega}_f - \omega^*) - \boldsymbol{A}_f\boldsymbol{\Omega} \tag{2a}$$

$$\frac{\mathrm{d}\boldsymbol{e}_f}{\mathrm{d}t} = -\boldsymbol{\beta}_f(\boldsymbol{E}_f - \boldsymbol{E}_f^*) - \boldsymbol{B}_f(\boldsymbol{Q} \oslash \boldsymbol{Q}_n) \tag{2b}$$

Here, $\boldsymbol{\Omega}_f$ and $\boldsymbol{e}_f$ denote the control signals of the follower DERs; $\boldsymbol{\alpha}_f$, $\boldsymbol{\beta}_f$, $\boldsymbol{A}_f$ and $\boldsymbol{B}_f$ are control parameters, where $\boldsymbol{A}_f$ and $\boldsymbol{B}_f$ are block diagonal matrices so that each follower DER only communicates within its local microgrid; $\boldsymbol{Q}_n$ denotes the reactive power rating of DERs; $\oslash$ denotes the element-wise division.

Further, leader DER share information with the entire NMs:

$$\frac{\mathrm{d}\boldsymbol{\Omega}_l}{\mathrm{d}t} = -\boldsymbol{\alpha}_l(\boldsymbol{\omega}_l - \omega^*) - \boldsymbol{A}_l\boldsymbol{\Omega} - \boldsymbol{C}_l\boldsymbol{\Omega}_l \tag{3a}$$

$$\frac{\mathrm{d}\boldsymbol{e}_l}{\mathrm{d}t} = -\boldsymbol{\beta}_l(\boldsymbol{E}_l - \boldsymbol{E}_l^*) - \boldsymbol{B}_l(\boldsymbol{Q} \oslash \boldsymbol{Q}_n) - \boldsymbol{D}_l(\boldsymbol{Q}_l \oslash \boldsymbol{Q}_{n,l}) \tag{3b}$$

Here, $\boldsymbol{\Omega}_l$ and $\boldsymbol{e}_l$ denote the control signals of the leader DERs; $\boldsymbol{A}_l$ and $\boldsymbol{B}_l$ are block diagonal so that each leader DER does not communicate with the follower DERs in other microgrids; the control parameters $\boldsymbol{C}_l$ and $\boldsymbol{D}_l$ formulate the communications between different microgrids. The formulation of inner and outer control loops in Fig. 1 is further presented in Appendix A-A.

B. Formulation of Network Transients

Recently, the dynamics of line branches and loads is found playing an unexpectedly important role in the dynamic performance of microgrids [21]. Because the DER-dominated microgrids and NMs are usually featured by the fast inverter dynamics and the small values of network impedance, the network transients tend to have significant influence on the slower system modes [22]. Although simplifying the network dynamics into algebraic equations is acceptable for bulk power systems with large inertia, this would lead to overly optimistic assessment of the inverter-interfaced microgrids [23]. Those new findings thus motivate us to model the dynamics of the entire NMs. For instance, the dynamics of a constant impedance load can be described as:

$$\boldsymbol{L}_l\frac{\mathrm{d}\boldsymbol{i}_l}{\mathrm{d}t} = -\boldsymbol{r}_l\boldsymbol{i}_l + \omega_s\boldsymbol{I}_s\boldsymbol{L}_l\boldsymbol{i}_l + \boldsymbol{M}_l\boldsymbol{v} \tag{4}$$

where $\boldsymbol{i}_l$ denotes the DQ-axis load currents; $\boldsymbol{v}$ denotes the DQ-axis bus voltages; $\boldsymbol{r}_l$ and $\boldsymbol{L}_l$ respectively denote the matrices of load resistances and inductance; $\boldsymbol{I}_s = \left[\begin{smallmatrix} \boldsymbol{0} & \boldsymbol{I} \\ -\boldsymbol{I} & \boldsymbol{0} \end{smallmatrix}\right]$ is a constant matrix constructed by the identity matrix $\boldsymbol{I}$; $\boldsymbol{M}_l$ is the DQ-axis incidence matrix between power loads and buses. Appendix A-B additionally presents a detailed formulation for incorporating the generic power load models.

The dynamics in the NM branches can be models as:

$$\boldsymbol{L}_b\frac{\mathrm{d}\boldsymbol{i}_b}{\mathrm{d}t} = -\boldsymbol{r}_b\boldsymbol{i}_b + \omega_s\boldsymbol{I}_s\boldsymbol{L}_b\boldsymbol{i}_b + \boldsymbol{M}_b\boldsymbol{v} \tag{5}$$

where $\boldsymbol{i}_b$ denotes the DQ-axis branch current; $\boldsymbol{r}_b$ and $\boldsymbol{L}_b$ respectively denote the matrices of branch resistances and inductance; $\boldsymbol{M}_b$ is the DQ-axis incidence matrix between branches and buses.

Each DER is connected to the backbone feeder through a branch with the following dynamics:

$$\boldsymbol{L}_o\frac{\mathrm{d}\boldsymbol{i}_o}{\mathrm{d}t} = -\boldsymbol{r}_o\boldsymbol{i}_o + \omega_s\boldsymbol{I}_s\boldsymbol{L}_o\boldsymbol{i}_o + \boldsymbol{v}_o - \boldsymbol{M}_o\boldsymbol{v} \tag{6}$$

where $\boldsymbol{i}_o$ and $\boldsymbol{v}_o$ respectively denote the DQ-axis current outputs and voltages of the DERs; $\boldsymbol{r}_o$ and $\boldsymbol{L}_o$ respectively denote the resistances and inductance of the interconnection branch; $\boldsymbol{M}_o$ is the DQ-axis incidence matrix between DERs and buses.

At each bus of the NMs, the Kirchhoff's Current Law should be satisfied:

$$\mathbf{0} = \boldsymbol{M}_o^T \boldsymbol{i}_o - \boldsymbol{M}_l^T \boldsymbol{i}_l - \boldsymbol{M}_b^T \boldsymbol{i}_b \tag{7}$$

C. ODE-Enabled NMs Model

By assembling the differential equations of the DERs (i.e., (2), (3) and the control loops in Appendix A-A), power loads (4) and branches (5), as well as the algebraic equations of buses (7), the NMs model can be integrated as a set of differential algebraic equation (DAEs).

Denote $\boldsymbol{i} = [\boldsymbol{i}_o; \boldsymbol{i}_l; \boldsymbol{i}_b]$ and $\boldsymbol{z}$ as all the other differential state variables in the NMs model. Accordingly, the NMs model is abstracted as:

$$\dot{\boldsymbol{z}} = \boldsymbol{g}(\boldsymbol{i}, \boldsymbol{z}, \boldsymbol{u}) \tag{8a}$$

$$\dot{\boldsymbol{i}} = \boldsymbol{A}\boldsymbol{v} + \boldsymbol{h}(\boldsymbol{i}, \boldsymbol{z}) \tag{8b}$$

$$\mathbf{0} = \boldsymbol{B}\boldsymbol{i} \tag{8c}$$

where (8a) is an abstraction of (2), (3) and (27); (8b) is an abstraction of (4), (5) and (6); (8c) is an abstraction of (7). The expression of $\boldsymbol{A}$, $\boldsymbol{B}$, $\boldsymbol{g}$ and $\boldsymbol{h}$ can be readily obtained from the NMs model, and the details are presented in Appendix A-C.

In the following, a fully ODE-based NMs model is devised by a rigorous DAE to ODE conversion. Denote the index set of maximal linearly independent columns of $\boldsymbol{B}$ as s_1, and that of other columns as s_0. Construct $\boldsymbol{B}_1$ with the columns of $\boldsymbol{B}$ corresponding to s_1, and $\boldsymbol{B}_0$ with the columns corresponding to s_0. Construct $\boldsymbol{i}_1$ with the elements of $\boldsymbol{i}$ corresponding to s_1, and $\boldsymbol{i}_0$ with the elements corresponding to s_0. Obviously, $\boldsymbol{B}_1$ is non-singular. Hence, (8c) yields the following:

$$\boldsymbol{i}_1 = -\boldsymbol{B}_1^{-1}\boldsymbol{B}_0\boldsymbol{i}_0 \tag{9}$$

Substituting (9) into (8) leads to the following:

$$\dot{\boldsymbol{z}} = \hat{\boldsymbol{g}}(\boldsymbol{i}_0, \boldsymbol{z}, \boldsymbol{u}) \tag{10a}$$

$$\dot{\boldsymbol{i}}_0 = \boldsymbol{A}_0\boldsymbol{v} + \hat{\boldsymbol{h}}_0(\boldsymbol{i}_0, \boldsymbol{z}) \tag{10b}$$

$$\dot{\boldsymbol{i}}_1 = \boldsymbol{A}_1\boldsymbol{v} + \hat{\boldsymbol{h}}_1(\boldsymbol{i}_0, \boldsymbol{z}) \tag{10c}$$

where $\hat{\boldsymbol{g}}(\boldsymbol{i}_0, \boldsymbol{z}) = \boldsymbol{g}(\boldsymbol{i}_0, \boldsymbol{i}_1, \boldsymbol{z})$ by substituting (9); $\hat{\boldsymbol{h}}(\boldsymbol{i}_0, \boldsymbol{z}) = \boldsymbol{h}(\boldsymbol{i}_0, \boldsymbol{i}_1, \boldsymbol{z})$; $\hat{\boldsymbol{h}}_0$ and $\hat{\boldsymbol{h}}_1$ respectively extract the elements of $\hat{\boldsymbol{h}}$ corresponding to $\boldsymbol{i}_0$ and $\boldsymbol{i}_1$.

Left-multiplying (8b) with $\boldsymbol{B}$ and substituting (9) give:

$$\mathbf{0} = \boldsymbol{B}\dot{\boldsymbol{i}} = \boldsymbol{N}\boldsymbol{v} + \boldsymbol{B}\hat{\boldsymbol{h}}(\boldsymbol{i}_0, \boldsymbol{z}) \tag{11}$$

where $\boldsymbol{N} = \boldsymbol{B}\boldsymbol{A}$.

If $\boldsymbol{N}$ is non-singular, the algebraic variables $\boldsymbol{v}$ can be expressed by the differential variables $(\boldsymbol{i}_0, \boldsymbol{z})$ as $\boldsymbol{v} = -\boldsymbol{N}^{-1}\boldsymbol{B}\hat{\boldsymbol{h}}$. Substituting $\boldsymbol{v}$ into (10) yields a full ODE model rigorously equivalent to the original DAE model in (8):

$$\dot{\boldsymbol{z}} = \hat{\boldsymbol{g}}(\boldsymbol{i}_0, \boldsymbol{z}, \boldsymbol{u}) \tag{12a}$$

$$\dot{\boldsymbol{i}}_0 = -\boldsymbol{A}_0\boldsymbol{N}^{-1}\boldsymbol{B}\hat{\boldsymbol{h}}(\boldsymbol{i}_0, \boldsymbol{z}) + \hat{\boldsymbol{h}}_0(\boldsymbol{i}_0, \boldsymbol{z}) \tag{12b}$$

If $\boldsymbol{N}$ is singular, it can be proved that (8) degenerates to an equivalent DAE model of a lower order. Then the above conversion can still be implemented.

No approximation or linearization is introduced in the above derivation, which theoretically ensures the efficacy of the ODE-enabled NMs model under large disturbances. Moreover, the DAE-ODE conversion processes the network current flow equations without affecting the interior models of the DERs and loads. Hence, the ODE-based model can readily accommodate arbitrary sources (e.g., DERs, synchronous and asynchronous machines), DER controls (e.g., PQ control, current control, voltage control, secondary control, etc), and loads (e.g., ZIP loads, electric motors).

The scale of the ODE-enabled NMs model mainly depends on the number of the DERs and loads rather than the size of the NM grid benefiting from the network sparsity feature, which therefore renders the ODE model improved efficiency. Moreover, solving the ODE-based models are numerically more stable than solving the DAE counterparts [24].

III. Reachable Dynamics of Disturbed NMs

A. Reachable Set of NMs With Dynamic Transitions

This Subsection integrates the hybrid automaton model used for the verification of a discrete-event system with the ODE model used for the reachability analysis of the NM dynamics. The flexibility afforded by this generalized reachability model enables the accurate modeling of arbitrary disturbances in the form of either parametric changes (e.g., frequent or sharp load fluctuations) or structural changes (e.g., plug-and-play of DERs or microgrids).

An extended state vector $\boldsymbol{x} = [\boldsymbol{z}; \boldsymbol{i}_0; t]$ is introduced to include the time information t in the NMs dynamics. The ODE-enabled, nonlinear dynamic model (12) is augmented as:

$$\dot{\boldsymbol{x}} = \begin{bmatrix} \hat{\boldsymbol{g}}(\boldsymbol{i}_0, \boldsymbol{z}, \boldsymbol{u}) \\ -\boldsymbol{A}_0\boldsymbol{N}^{-1}\boldsymbol{B}\hat{\boldsymbol{h}}(\boldsymbol{i}_0, \boldsymbol{z}) + \hat{\boldsymbol{h}}_0(\boldsymbol{i}_0, \boldsymbol{z}) \\ 1 \end{bmatrix} = \boldsymbol{f}(\boldsymbol{x}, \boldsymbol{u}) \tag{13}$$

where the NMs state vector $\boldsymbol{x}$ is defined in the state space $\mathcal{X} \subseteq \mathbb{R}^n$; the DER uncertainty vector $\boldsymbol{u}$ is defined in the input space and governed by an unknown-but-bounded set $\mathcal{U} \subseteq \mathbb{R}^m$.

Given a set of disturbance events $\mathcal{D} = \{D_1, D_2, \ldots, D_K\}$, the NMs dynamics is discretely divided into K modes $\mathcal{Y} = \{y_1, y_2, \ldots, y_K\}$. Upon the occurrence of a disturbance D_j, an NMs system operating in its current mode y_i would undergo a transition $y_i \to y_j$. Correspondingly, the NMs dynamics with disturbance transients can be modelled as a hybrid automaton:

$$H = (\mathcal{X}^0, \mathcal{U}^0, \mathcal{Y}, \mathcal{D}, E, \boldsymbol{f}, T) \tag{14}$$

Here, $\mathcal{X}^0 \subseteq \mathcal{X}$ denotes the set of the NMs initial states corresponding to the initial mode y_0; $\mathcal{U}^0 \subseteq \mathcal{U}$ denotes the set of the DER uncertainties; $\mathcal{D}$ and $\mathcal{Y}$ respectively denotes the disturbance set and mode set as defined above; $E = \{(t_1, y_{e_1}), (t_2, y_{e_2}), \ldots, (t_S, y_{e_S})\}$ denotes the time-series events triggering the NMs' transitions to y_{e_s} at time t_s; the dynamic function $\boldsymbol{f} : \mathcal{X} \times \mathcal{U} \times \mathcal{Y} \to \mathcal{X}$ formulates the ODE-enabled NMs model under each mode, as detailed in (13); the transition function $T : \mathcal{X} \times \mathcal{U} \times \mathcal{Y} \times \mathcal{Y} \to \mathcal{X} \times \mathcal{U}$ formulates the transition process from one mode to another, whose outputs

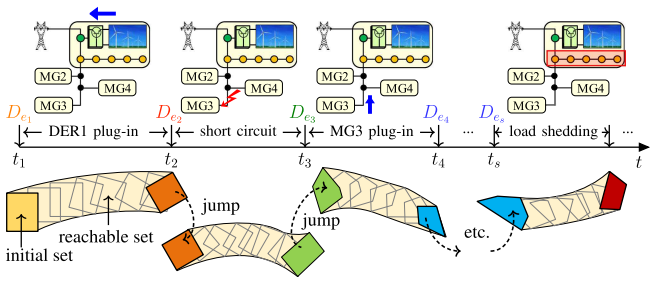

Fig. 2. Illustration of the reachable set transition with disturbances in NMs.

are the sets of NMs states and DER uncertainties in the succeeding mode when the transition occurs:

$$(\mathcal{X}_j^0, \mathcal{U}_j^0) =: T(\mathcal{X}_i^{end}, \mathcal{U}_i^0, y_i, y_j)$$
$$= (\boldsymbol{M}_{(y_i,y_j)}\mathcal{X}_i^{end} + \boldsymbol{m}_{(y_i,y_j)}, \boldsymbol{N}_{(y_i,y_j)}\mathcal{U}_i^0 + \boldsymbol{n}_{(y_i,y_j)}) \quad (15)$$

where y_i associating y_j describes the NMs' structural/parametric transition $y_i \to y_j$; $\mathcal{X}_j^0$ and $\mathcal{U}_j^0$ respectively denote the initial set of NMs' states and DER uncertainties in mode y_j; $\mathcal{X}_i^{end}$ denotes the set of NMs states in mode y_i at the time point of transition; $\boldsymbol{M}_{(y_i,y_j)}$, $\boldsymbol{m}_{(y_i,y_j)}$, $\boldsymbol{N}_{(y_i,y_j)}$, $\boldsymbol{n}_{(y_i,y_j)}$ are specific transition matrices for $y_i \to y_j$.

By using the hybrid automaton defined in (14), the NMs' structural/parametric transitions under large disturbances are incorporated in the reachability analysis. The reachable set of the NMs states at time t is defined as a set of all the possible $x(t)$ given the initial states $\mathcal{X}^0$ and uncertain input $\mathcal{U}$:

$$\hat{\mathcal{R}}(t) = \Big\{ \boldsymbol{x}(t) \;\Big|\; (\boldsymbol{x}(t), \boldsymbol{u}(t), \boldsymbol{y}(t)) \text{ is a solution of } H,$$
$$\boldsymbol{x}(0) \in \mathcal{X}^0, \boldsymbol{u}([0,t]) \in \mathcal{U}, y(0) = y_0 \Big\} \quad (16)$$

Further, the NMs reachable set during time interval $[t, t+\Delta t]$ is defined as a union of the discrete-time reachable sets:

$$\hat{\mathcal{R}}([t, t+\Delta t]) = \cup_{\tau \in [t, t+\Delta t]} \hat{\mathcal{R}}(\tau) \quad (17)$$

Fig. 2 illustrates the transitions of the NMs reachable set. A disturbance sequence including plugging-in of DER/microgrid, short-circuit and load shedding is taken as an example. Upon each disturbance, the NMs transitions from the current structure/parameters to another, which induces the reachable set's jump from the current state space to a new one. Further, during the time intervals in which no transition occurs, with the initial state set, the continuous reachable set is calculated to enclose all the possible NMs trajectories in the specific mode (see Section II-C). The hybrid automaton-empowered reachability methodology therefore can handle the NMs dynamic transitions between large disturbances superimposed on other uncertainties and is applicable to single contingencies as well multiple contingencies.

B. Set Representation Via Zonotope Bundles

Reachability analysis performs set computation to verify the system dynamics. Recently, zonotope has been adopted in microgrid reachability analysis for the quasi-static states [18]. Despite the high computational efficiency, zonotope has inherent deficiencies such as: 1) it has a special and restricted structure (i.e., centrally symmetric polytope) and 2) it is not closed under several set computations (e.g., intersection). Those deficiencies introduce escalated over-approximations in NMs set computations, causing low-precision and ill-convergence issues in the reachability analysis of highly nonlinear dynamics. To tackle the challenge, a new set representation, i.e., the zonotope bundle, is employed to enable a highly precise and efficient reachability analysis of NMs with large disturbances.

The zonotope bundle is defined as the intersection of a finite number of zonotopes [25]:

$$\mathcal{Z}^{\cap} = \cap_{i=1}^{n} \mathcal{Z}_i \quad (18)$$

Here, $\mathcal{Z}_i$ denotes a zonotope defined by its center $\boldsymbol{c}$ and K generators $(\boldsymbol{g}^{(1)}, \ldots, \boldsymbol{g}^{(K)})$ such that $\mathcal{Z}_i = \{\boldsymbol{x} \in \mathbb{R}^n | \boldsymbol{x} = \boldsymbol{c} + \sum_{k=1}^{K} \beta_k \boldsymbol{g}^{(k)}, |\beta_k| \le 1\}$.

Zonotope bundle is able to represent arbitrary polytopes (convex and bounded), and hence is far more flexible for uncertainty formulations. Moreover, zonotope bundle is closed under intersection, which enables improved accuracy in set computations. A comparative study has reported the efficacy of using zonotope bundles in verifying nonlinear systems together with cases where zonotopes fail to capture the dynamics [25].

C. Reachability Analysis Via Zonotope Bundles

Calculating the exact reachable set is computational intractable. Instead, a rigorously over-approximated reachable set $\hat{\mathcal{R}}(t)$ satisfying $\hat{\mathcal{R}}(t) \subseteq \mathcal{R}(t)$ is sufficient for verifying the system dynamics with a moderate computational cost.

At each time point, the NMs dynamic model (13) is over-approximated by the Taylor series expansion:

$$\dot{\boldsymbol{x}} \in \boldsymbol{f}(\boldsymbol{x}^*, \boldsymbol{u}^*) + \boldsymbol{J}(\boldsymbol{x} - \boldsymbol{x}^*) + \boldsymbol{J}_u(\boldsymbol{u} - \boldsymbol{u}^*) + \boldsymbol{L}(\boldsymbol{x}, \boldsymbol{u}) \quad (19)$$

where $\boldsymbol{x}^*$ and $\boldsymbol{u}^*$ respectively denote the linearization point of the NMs states and DER uncertainties; $\boldsymbol{J} = \partial \boldsymbol{f}(\boldsymbol{x}^*, \boldsymbol{u}^*)\boldsymbol{x}$ and $\boldsymbol{J}_u = \partial \boldsymbol{f}(\boldsymbol{x}^*, \boldsymbol{u}^*)/\partial \boldsymbol{u}$ respectively denote the Jacobian matrices of the NMs; $\boldsymbol{L}$ denotes the Lagrange remainder:

$$\boldsymbol{L}(\boldsymbol{x}, \boldsymbol{u}) = \frac{1}{2}[\boldsymbol{x} - \boldsymbol{x}^*; \boldsymbol{u} - \boldsymbol{u}^*]^T \frac{\partial^2 \boldsymbol{f}(\boldsymbol{\xi_x}, \boldsymbol{\xi_u})}{\partial [\boldsymbol{x}; \boldsymbol{u}]^2} [\boldsymbol{x} - \boldsymbol{x}^*; \boldsymbol{u} - \boldsymbol{u}^*] \quad (20)$$

where $\xi_x \in \{\boldsymbol{x}^* + \alpha(\boldsymbol{x} - \boldsymbol{x}^*) | \alpha \in [0,1]\}$, $\xi_u \in \{\boldsymbol{u}^* + \alpha(\boldsymbol{u} - \boldsymbol{u}^*) | \alpha \in [0,1]\}$. The Taylor's Theorem [26] ensures that for arbitrary $\boldsymbol{x}$ and $\boldsymbol{u}$, there exist ξ_x and ξ_u so that the nonlinear function $\boldsymbol{f}$ can be formulated by the first-order Taylor polynomial and the error terms $\boldsymbol{L}(\boldsymbol{x}, \boldsymbol{u})$. Therefore, calculating $\boldsymbol{L}$ by the set of $\boldsymbol{x}$ and $\boldsymbol{u}$ can ensure that (20) rigorously encloses arbitrary $\dot{\boldsymbol{x}}$. In the following derivation, the center of $\mathcal{U}$ is assumed as the origin point without loss of generality. Meanwhile, $\mathcal{R}(t)$ is shifted to $\mathcal{R}(t) - \boldsymbol{x}^*$ to eliminate the impact of the linearization point and is shifted back at the end of set calculations.

Accordingly, the reachable set of the linearized NMs model can be obtained:

$$\mathcal{R}(t + \Delta t) = \left(e^{\boldsymbol{J}\Delta t}\mathcal{R}(t)\right) \oplus \mathcal{R}^u(\Delta t) \oplus \mathcal{R}^{err} \quad (21)$$

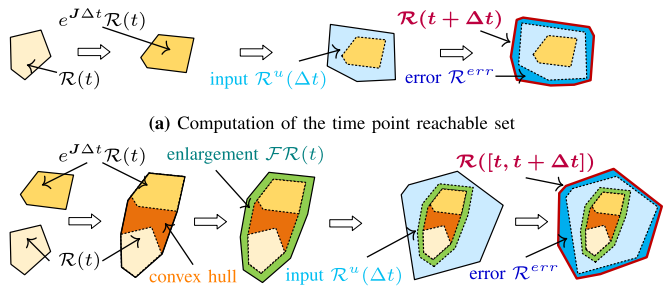

(a) Computation of the time point reachable set

(b) Computation of the time interval reachable set

Fig. 3. Illustration of reachable set computation.

Here, Δt denotes the time step; $\oplus$ denotes the Minkowski addition of two zonotope bundles, which is performed as:

$$\mathcal{Z}_1^{\cap} \oplus \mathcal{Z}_2^{\cap} =: (\cap_{i=1}^{n} \mathcal{Z}_i^{(1)}) \oplus (\cap_{j=1}^{m} \mathcal{Z}_j^{(2)}) \subseteq \{\mathcal{Z}_1^{(1)} \oplus \mathcal{Z}_1^{(2)}, \ldots, \mathcal{Z}_n^{(1)} \oplus \mathcal{Z}_1^{(2)}, \ldots, \mathcal{Z}_n^{(1)} \oplus \mathcal{Z}_m^{(2)}\}^{\cap} \quad (22)$$

Fig. 3(a) illustrates the computing step of (21). In (21), the first term refers to the response to $\boldsymbol{J}(\boldsymbol{x}-\boldsymbol{x}^*)$, i.e., the NMs states. The second term refers to the response to the inputs [27], which is the impact of DER uncertainties $\mathcal{U}$ as well as the linearization point:

$$\mathcal{R}^u(\Delta t) = \sum_{i=0}^{\eta} \left(\frac{\boldsymbol{J}^i (\Delta t)^{i+1}}{(i+1)!} \mathcal{U}_f \right) \oplus \mathcal{E}(\Delta t) \mathcal{U}_f \Delta t \quad (23)$$

where $\mathcal{U}_f = \boldsymbol{J}_u(\mathcal{U}-\boldsymbol{u}^*) + \boldsymbol{f}(\boldsymbol{x}^*, \boldsymbol{u}^*)$; η is the number of Taylor terms; $\mathcal{E}(\Delta t) = [-\mathbf{1}, \mathbf{1}] \frac{(J_\infty \Delta t)^{\eta+1}}{(\eta+1)!} \frac{1}{1-\epsilon}$ denotes the Taylor expansion remainder after η terms [28]. And the third term in (21) refers to the linearization error due to the Lagrange remainder [29].

Further, the reachable set of NMs state during each time-interval can be obtained from the discrete-time sets:

$$\mathcal{R}([t, t+\Delta t]) = \mathbf{Conv}(\mathcal{R}(t), e^{\boldsymbol{J}\Delta t}\mathcal{R}(t)) \oplus \mathcal{F}\mathcal{R}(t) \oplus \mathcal{R}^u(\Delta t) \oplus \mathcal{R}^{err} \quad (24)$$

Here, the operator $\mathbf{Conv}(\cdot,\cdot)$ denotes the convex hull enclosure of a zonotope bundle and its linear mapping, which is performed as:

$$\mathbf{Conv}(\mathcal{Z}^{\cap}, M\mathcal{Z}^{\cap}) =: \mathbf{Conv}(\cap_{i=1}^{n} \mathcal{Z}_i, M \cap_{i=1}^{n} \mathcal{Z}_i) \subseteq \{\mathbf{Conv}(\mathcal{Z}_1, M\mathcal{Z}_1), \ldots, \mathbf{Conv}(\mathcal{Z}_n, M\mathcal{Z}_n)\}^{\cap} \quad (25)$$

Fig. 3(b) illustrates the computing process of (24). In (24), the first two terms together approximate the set at each time point during the interval through an interpolation below:

$$\boldsymbol{x}(t+\tau) \in \boldsymbol{x}(t) + \frac{\tau}{\Delta t}(e^{\boldsymbol{J}\Delta t} - \boldsymbol{I})\boldsymbol{x}(t) + \mathcal{F}\boldsymbol{x}(t), \tau \in [0, \Delta t] \quad (26)$$

where the interval matrix $\mathcal{F} = \sum_{i=2}^{\eta} [(i^{\frac{-i}{i-1}} - i^{\frac{-1}{i-1}})\Delta t^i, 0] \frac{\boldsymbol{J}^i}{i!} \oplus \mathcal{E}(\Delta t)$ enlarges the reachable set to ensure the necessary conservativeness. The third term in (24) refers to the reachable set in response to the DER uncertainties as calculated in (23) and the forth term is the Lagrange remainder.

Algorithm 1: Reachable dynamics algorithm of NMs with disturbance transients

▷ ***Initialization***: set of initial NMs states $\mathcal{R}(t) = \mathcal{X}^0$, set of DER uncertainties $\mathcal{U} = \mathcal{U}^0$, $y = y_0$, $t = t_{\text{start}}$;
while $t \le t_{end}$ **do**
  ▷ ***NMs Structure Transition***:
  if $t \in \{t_1, t_2, \cdots, t_S\}$ **then**
    transition from $y_i (i \in \{i | y_i = y\})$ to $y_j (j \in \{j | t_s = t, j = e_s\})$:
    $\mathcal{R}(t) = \boldsymbol{M}_{(y_i,y_j)}\mathcal{R}(t) + \boldsymbol{m}_{(y_i,y_j)}$;
    $\mathcal{U} = \boldsymbol{N}_{(y_i,y_j)}\mathcal{U} + \boldsymbol{n}_{(y_i,y_j)}$;
    $y = y_j$; $\boldsymbol{f} = \boldsymbol{f}_j$;
  end
  ▷ ***NMs State Set Calculation***:
  linearization at $\boldsymbol{x}^* = \mathrm{c}(\mathcal{R}(t)) + \frac{1}{2}\boldsymbol{f}(\mathrm{c}(\mathcal{R}(t)), \mathrm{c}(\mathcal{U}))\Delta t$, $\boldsymbol{u}^* = \mathrm{c}(\mathcal{U})$;
  computation of $\mathcal{R}(t+\Delta t)$ and $\mathcal{R}([t, t+\Delta t])$ by (21) and (24) ;
  result evolution $\mathcal{R}_{(tp)} = \{\mathcal{R}_{(tp)}, \mathcal{R}(t+\Delta t)\}$, $\mathcal{R}_{(ti)} = \{\mathcal{R}_{(ti)}, \mathcal{R}([t, t+\Delta t])\}$;
  time evolution $t = t + \Delta t$;
end
▷ ***Output***: time-point reachable sets $\mathcal{R}_{(tp)}$; time-interval reachable sets $\mathcal{R}_{(ti)}$;

D. Overall Procedure

Algorithm 1 establishes the complete procedures for reachable dynamics analysis of NMs under disturbances.

- *Initialization:* After loading in the NMs parameters, uncertainty parameters and disturbance information, the routine starts at t_{start} with the initialized zonotope bundles of the NMs states and DER uncertainties, i.e., $\mathcal{X}^0$ and $\mathcal{U}^0$, as well as the initial NMs structure y_0.
- *NMs structure transition:* If a transition from the current mode y_i to the new mode y_j is triggered, the initial set of NMs states for mode y_j is computed by the transition function T in (15).
- *NMs state set calculation:* After the reachable set is transitioned, the continuous reachable set of NMs in the current mode is computed by the algorithm in Section III-C, with the linearization point $\boldsymbol{x}^* = \mathrm{c}(\mathcal{R}(t)) + \frac{1}{2}\boldsymbol{f}(\mathrm{c}(\mathcal{R}(t)), \mathrm{c}(\mathcal{U}))\Delta t$, $\boldsymbol{u}^* = \mathrm{c}(\mathcal{U})$ (operator $c(\cdot)$ retrieves the center of the zonotope bundle).

IV. Case Study

This section demonstrates the technical merit and efficacy of the reachable dynamics analysis for NMs. The new method is tested under typical large disturbances (i.e., load shedding, fault, DER plug-and-play) taking into consideration of droop and secondary control strategies of DERs. The algorithm is implemented in MATLAB R2019b.

A. Technical Merit

The technical merit of the ODE-based, zonotope bundle-empowered reachability analysis is demonstrated through dynamic verification of a typical microgrid detailed in [30].

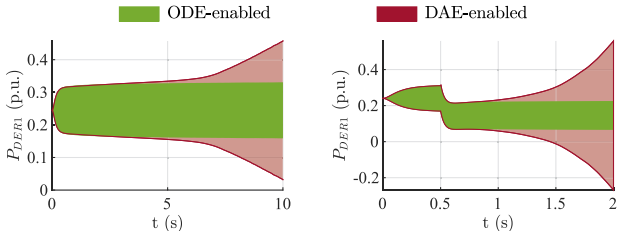

(a) Case 1: no-fault **(b)** Case 2: load shedding

Fig. 4. Comparison of the reachable sets obtained from the DAE-enabled and ODE-enabled reachability algorithms.

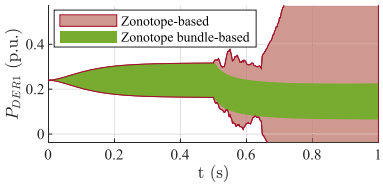

Fig. 5. Comparison of the reachable dynamics results using zonotopes and zonotope-bundles.

1) Necessity of Adopting ODE-Enabled Reachability Analysis: Case 1 is a quasi-static 'flat-start' scenario where the microgrid remains stable and the time-domain trajectories reach the steady states shortly. Fig. 4(a) compares the performance of the DAE model with the ODE model under 20% uncertainties from DERs, where both models produce similar results during the first 5 seconds. However, the DAE-enabled reachability calculation diverges after 5 s, failing to capture the true dynamic behavior of the microgrid. In contrast, the ODE-enabled algorithm reaches a steady reachable set and accurately encloses the uncertain microgrid states. The reason behind the divergence of the DAE-based reachability computing is that the uncertainty effect is over-approximated during the interactions between the sets of differential states and algebraic states to ensure conservativeness, which inevitably causes error accumulations during iterations.

Case 2 is to compare both methods with 30% of the loads tripped at 0.5 s. Fig. 4(b) shows that the reachable set obtained from the DAE-based reachability analysis begins to diverge after 1 s, indicating that the numerical instability of the DAE-based algorithm is even worse under a large disturbance. The ODE-enabled reachable dynamics analysis enhanced by using zonotope bundles again exhibits excellent numerical stability under a large disturbance. Correctness of the ODE-enabled algorithm will be further demonstrated in the following.

2) Necessity of Using Zonotope Bundles: Fig. 5 compares the performances of using zonotopes and zonotope bundles in the ODE-enabled formal analysis. Simulation shows that zonotope-based calculation does not survive the 30% load-shedding disturbance, while zonotope-bundle still catches the fast nonlinear dynamics after the large disturbance.

B. NMs Dynamic Verification Via Reachable Dynamics

This Subsection studies the NMs dynamics with both large disturbances and uncertain perturbations via reachability analysis. Tests are conducted on a 4-microgrid NMs with the topology presented in Fig. 1. Detailed parameters of the test system are presented in Appendix B. The test system is a medium-sized networked microgrid with 5 DERs, 28 power loads and 32 branches, which leads to a 98-dimensional ODE model. The default uncertainty level of each DER is set as 20%.

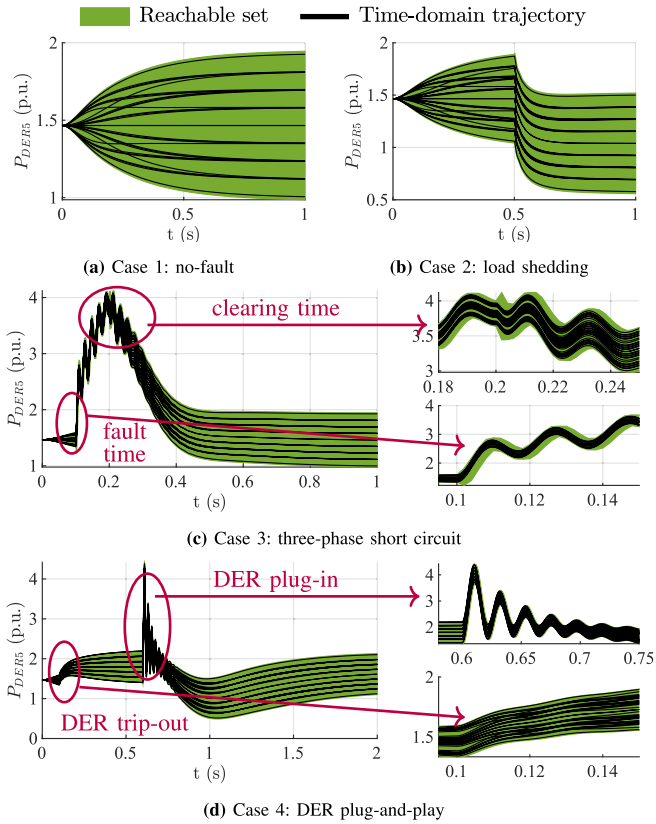

(a) Case 1: no-fault **(b)** Case 2: load shedding

(c) Case 3: three-phase short circuit

(d) Case 4: DER plug-and-play

Fig. 6. Reachable dynamics vs Monte Carlo time-domain trajectories.

1) Validity of Reachability Analysis: Fig. 6 compares the NMs reachable sets with the time-domain trajectories obtained by the trapezoidal rule of integration [31]. Four typical cases are considered: i) **Case 1**: No fault but only the DER uncertainty applies; ii) **Case 2**: 30% load shedding occurs at 0.5 s and the NMs load remains unrecovered; iii) **Case 3**: A three-phase-to-ground fault occurs at 0.1 s and is cleared at 0.2 s; and iv) **Case 4**: DER1 is tripped at 0.1 s and reconnected at 0.6 s.

It should be noted that this paper considers the balanced three-phase faults and does not include the relay protection operations. Future work will be extended to include the formal verification of unbalanced systems and protection behaviors.

In all the cases, the reachable sets well replicate both the quasi-static states (i.e., the NMs dynamics only impacted by the DER uncertainties) and the fast dynamics during disturbances. In particular, the reachable sets securely enclose all the time-domain trajectories with tight reachability bounds. Specifically, Fig. 6(c) and Fig. 6(d) magnify the reachable set during the short periods from the fault occurrence through the fault clearance, which illustrate the excellent performance of the new method in capturing the NMs transients initiated by large disturbances.

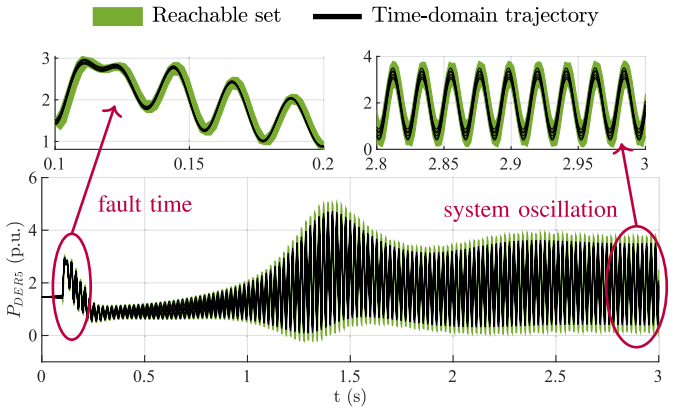

Fig. 7. Reachable dynamics for an unstable case under three-phase short circuit.

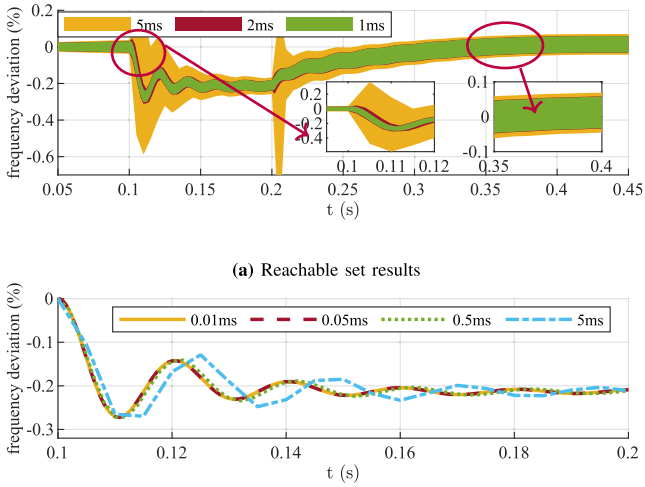

(a) Reachable set results

(b) Time-domain simulation results

Fig. 8. Reachable set result with different time step and its comparison with time-domain simulation with trapezoidal rule.

Further, Fig. 7 demonstrates the reachable dynamics for an unstable case (i.e., DERs are set with destabilizing droop coefficients) under three-phase short circuit fault occurring at 0.1 s and cleared at 0.2 s. Time-domain simulation shows that the improper droop settings induces severe oscillation after the fault occurs. Meanwhile, the reachable sets perfectly capture the NMs dynamics and tightly enclose the rapidly oscillating time-domain trajectories, exhibiting the capability of the reachable dynamics approach in handling unstable scenarios.

In sum, simulation results in Fig. 6 and Fig. 7 verify the capability of the reachable dynamics method in rigorously enclosing the uncertain time-domain trajectories under small perturbations, large disturbances as well as unstable scenarios.

Compared with the randomized time-domain simulation (the most commonly-used approach for analyzing the system dynamics under uncertainties), an outstanding feature of the reachability analysis is that it calculates a conservative set of an infinite number of possible trajectories in one simulation run. Yet another interesting finding is the unexpected high robustness of the reachable dynamics analysis. Usually, a very small time step is required for a step-by-step time-domain simulation to capture fast dynamics precisely. As presented in Fig. 8(b), a time step less than 0.05 ms is required for a reasonably accurate time-domain simulation of a three-phase fault in the test NMs. Otherwise, the frequency excursions would be inaccurate, which can be hazardous in system operations or planning. As for the reachability analysis, a large time step only leads to overly conservative result (see Fig. 8(a)). Although the impact of disturbance is overestimated, it would not bring in catastrophic effect due to negligence of potentially dangerous cases because the result is still rigorously credible and can enclose all possible hazards. As Fig. 8(a) indicated, a 2 ms time-step already leads to satisfactory result with respect to tightness, and a 5 ms time-step is sufficient for the slow dynamics scenario. Table. I further presents the time consumption for calculating reachable dynamics during [0 s,1s]. Two test systems are studied: a single microgrid [30] (i.e., a microgrid with 3 DERs and 2 power loads), and the networked microgrid in Fig. 1 (i.e., an NMs with 4 microgrids, 5 DERs and 28 power loads). For comparison purpose, the computing times

TABLE I
COMPUTING TIME OF REACHABLE DYNAMICS

Test system	Time step	Reachable dynamics run time	Time step	Time-domain simulation (30 runs)
A single microgrid	5ms	6.63s	5ms	12.29s
	2ms	16.51s	0.5ms	62.92s
	1ms	33.45s	0.05ms	540.52s
Networked microgrids	5ms	61.13s	5ms	38.53s
	2ms	142.64s	0.5ms	308.34s
	1ms	270.08s	0.05ms	2961.32s

of time-domain simulations are also presented. Fig. 8(a) shows that, to obtain a precise enough time-domain simulation, a time step no more than 0.5 ms is required. Meanwhile, to address the uncertain dynamics behaviors, it needs to perform numerous Monte Carlo runs of time-domain simulations. Table. I shows that the computing time for reachable dynamics is acceptable for off-line analysis and is more efficient than a very light Monte Carlo simulation of 30 runs. Denote n as the system dimension and n_u as the dimension of uncertainties. Theoretically, traversing the uncertainty space while performing step-by-step time-domains simulation leads to a computational complexity of at least $o(p^{n_u}) \times o(\text{poly}(n))$ at each time point (here, p is the sampling number of each dimension of the uncertainty vector $\boldsymbol{u}$; $o(\text{poly}(n))$ is the complexity of a nonlinear/linear equation solver [32]). In spite of the numerical difficulties, this traversing can still fail to ensure an reliable estimation of the transient risks under uncertainties because the infinite possible scenarios can never be enumerated. In contrast, the reachable dynamics method has a worst complexity of $o(n^5)$ according to the reachability analysis theory [29] as well as well as ensures a provable conservative result.

2) Observations From Reachable Dynamics Analysis of NMs:

i) Case 1: No fault but the DER uncertainty disturbs the NMs. Fig. 9 illustrates frequency deviations and DER outputs under

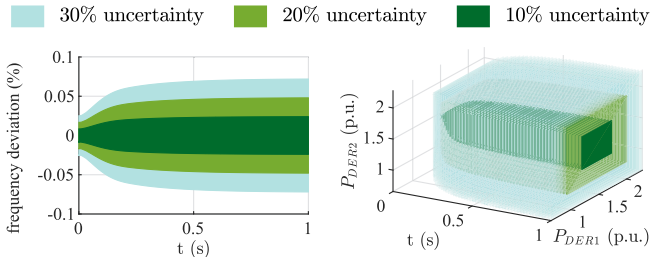

(a) System frequency **(b)** Active power of DERs

Fig. 9. Reachable set under different uncertainty level.

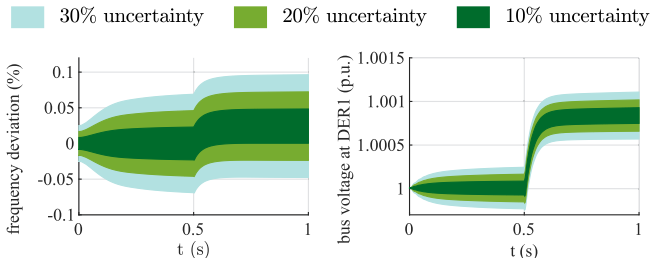

(a) System frequency **(b)** Bus voltage at DER1

Fig. 10. Reachability verification for load shedding dynamic under different uncertainty level.

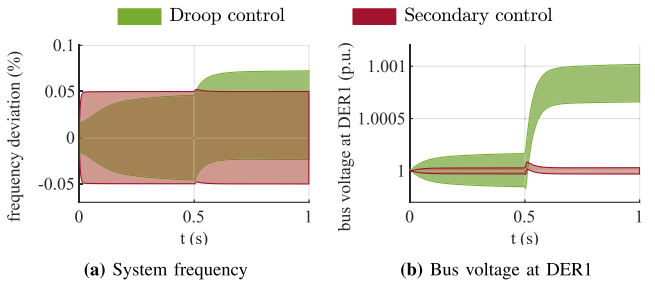

(a) System frequency **(b)** Bus voltage at DER1

Fig. 11. Control efficacy verification under load shedding disturbance.

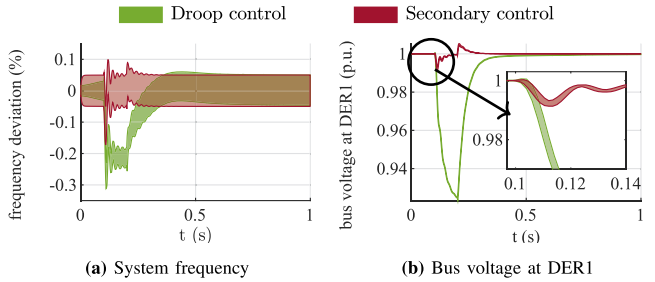

(a) System frequency **(b)** Bus voltage at DER1

Fig. 12. Control efficacy verification under three-phase short-circuit.

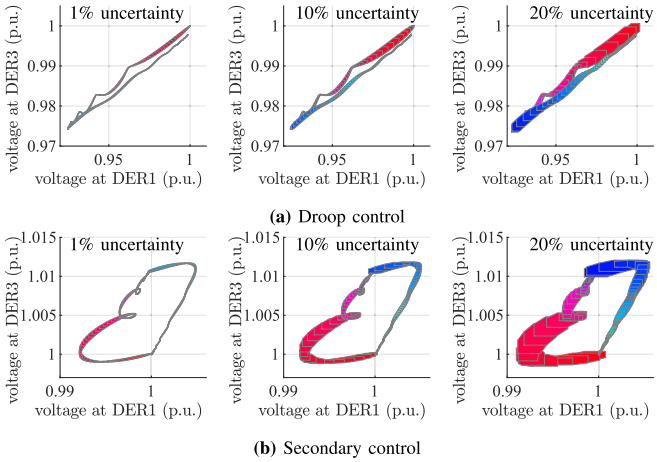

(a) Droop control

(b) Secondary control

Fig. 13. State-space reachable set under three-phase short circuit.

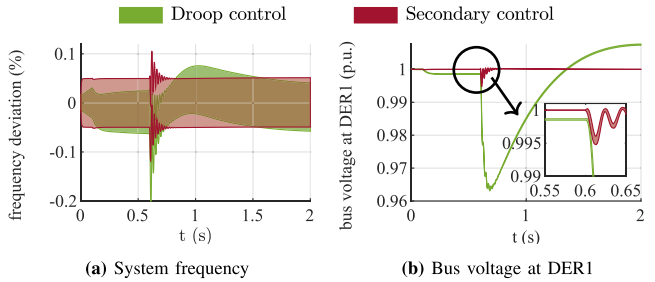

(a) System frequency **(b)** Bus voltage at DER1

Fig. 14. Control efficacy verification under DER's plug-and-play.

three levels of uncertainties, where the two reachable sets expand with the increase of uncertainty level.

Ii) Case 2: Disturbance caused by permanent load shedding. Fig. 10 presents the reachtubes of frequency and voltage excursions after the load shedding. Further, Fig. 11 compares the efficacy of droop control and secondary control. Compared with the case with the droop control only, the secondary control exhibits outstanding performance in rapidly stabilizing the system frequency and voltage fluctuation after load shedding through a speedy power sharing among DERs.

Iii) Case 3: Disturbance from a temporary three-phase fault. Fig. 12 shows that secondary control performs well for restraining the frequency/voltage overshoot and recovering the system state after large disturbance.

Fig. 13 further investigates the uncertainty impact on the the faulted NMs from a state-space perspective. Comparing between the system states at different uncertainty levels, the propagation of uncertainty in the NMs dynamics is distinctly revealed, which makes the randomized time-domain simulation unnecessary. Comparing the reachable sets with the droop and secondary controls, it is obvious that the NMs undergoes much smaller voltage dip with the secondary control.

Iv) Case 4: For the DER plug-and-play, both the NMs frequency and voltages should be carefully monitored due to the instantaneous deficiency/surplus of active and reactive power generation. Fig. 14 illustrates the reachable set evolution during [0 s, 2 s]. Besides the damped overshoot, the secondary control can also assist the NMs to reach a new steady-state faster. In contrast, when there is only droop control, DERs can not coordinate effectively to participate in the power regulation and to restore the system frequency and voltages. The state-space

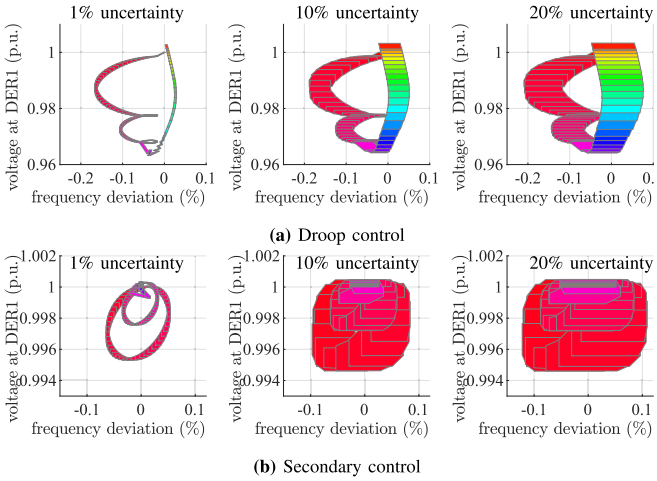

(a) Droop control

(b) Secondary control

Fig. 15. State-space reachable set under DER's plug-and-play.

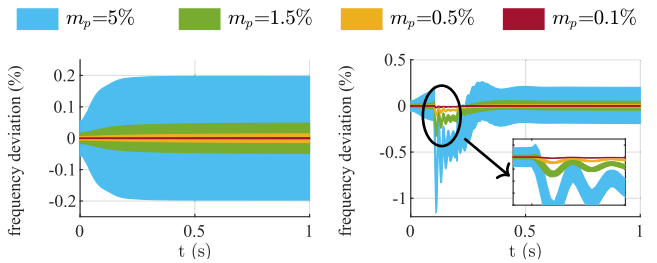

(a) Case 1: no-fault (b) Case 3: short-circuit

Fig. 16. Impact of active droop coefficient m_p on NMs reachable dynamics.

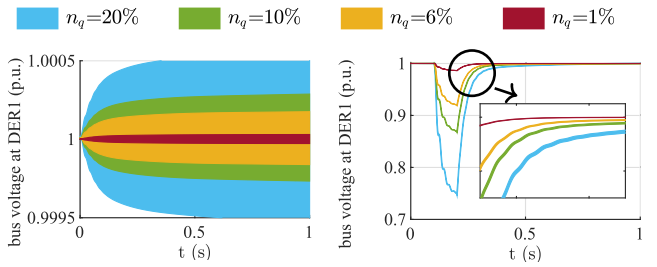

(a) Case 1: no-fault (b) Case 3: short-circuit

Fig. 17. Impact of reactive droop coefficient n_q on NMs reachable dynamics.

reachable sets in Fig. 15 further demonstrate the performance of droop/secondary control under different uncertainty levels.

C. Controller Performance Analysis Via Reachable Dynamics

This Subsection investigates the impact of controller settings on the uncertain NMs dynamics via reachability analysis.

1) Impact of Droop Control Parameters: Fig. 16 and Fig. 17 investigate the impact of droop control coefficients on the NMs reachable dynamics. In this test system, the active power droop gain m_p mainly influences the NMs' frequency response, while the reactive power droop gain n_q mainly influences the NMs' voltage response. Simulation results show that with the decrease of droop coefficients: i) the reachable sets of NMs frequency/voltage shrink under both no-fault scenario and large disturbance scenario, which indicates an enhanced robustness against the uncertainties; ii) the frequency/voltage dips are restrained and the NMs system reaches a new steady state more rapidly, which indicates an improved control efficacy of the droop controllers. Compared with the traditional time-domain simulation methods, the reachable dynamics approach not only reflects the NMs dynamic response under different controller parameters, but also reveals the capability of the controllers in handling the uncertainties during the transient process.

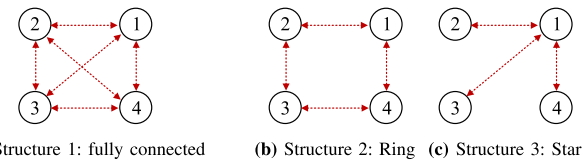

(a) Structure 1: fully connected (b) Structure 2: Ring (c) Structure 3: Star

Fig. 18. Communication structure for the test NMs.

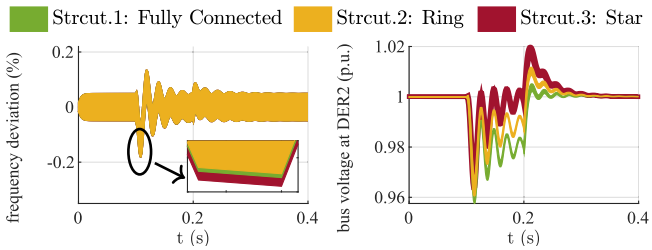

(a) System frequency (b) Bus voltage at DER2

Fig. 19. Impact of communication structure on NMs reachable dynamics.

2) Impact of Communication Structure: The NMs secondary control, as formulated by (2) and (3), requires the communication between microgrids to perform a global control. Three typical communication structures [33] between the 4 microgrids are studied, as presented in Fig. 18: i) **Structure 1-fully connected** (the default structure): microgrids 1–4 fully communicate with each other; ii) **Structure 2-Ring structure**: each microgrid only communicates with the neighboring microgrids; iii) **Structure 3-Star structure**: microgrid 1 serves as the central point and microgrids 2–4 separately get control signals from microgrid 1.

Reachable dynamics with different communication structures under a three-phase fault are presented in Fig. 19. For the frequency reachable sets, the Star structure leads to a larger frequency dip and the Ring structure leads to a larger frequency overshoot, but the difference of the NM performance between the structures is very slight. As for the voltage reachable sets, the fully connected structure causes the largest voltage dip while the Star structure causes the largest voltage overshoot. From the uncertainty perspective, the reachable set is narrowest under the fully connected structure and widest under the Star structure (i.e., the least connected structure), indicating that a more strongly connected communication network might help restrain the impact of uncertainties in the NMs. However, the simulation results above show that the impact of communication structures on the NMs dynamics is not as explicit as that of

droop coefficients. It is hard to distinguish which communication topology is better in terms of the overall effect when considering the frequency/voltage dynamics, uncertainty suppression, etc.

V. Conclusion

The paper devises a reachability analysis method to formally verify the fast and strongly-nonlinear dynamics of the inverter-dominated NMs. The key innovation lies in the integration of the ODE-enabled NMs model, the hybrid automaton theory for incorporating discrete large disturbances and the zonotope bundle-based set representation to provide a conservative, tight and convergent enclosure of all possible NMs dynamic trajectories under both uncertainty perturbation and large disturbances. Case studies of a typical NMs system verify the effectiveness of the established method. The reachable dynamics method, which formally assesses the impact of the heterogeneous uncertainties on the NMs transients, can assist the NMs operators to test the contingency dynamics (*i.e.*, N-1 or N-x) and verify the controller efficacy under both disturbances and uncertainties. Therefore, it can serve as a tool to effectively promote the reliability, stability and robustness of today's low-inertia and highly variable NMs. In the future, the protective relay behaviors against large disturbances will be incorporated in the reachability analysis scheme.

Appendix A
Remarks on ODE-Enabled NMs Model

A. Detailed DER Controller Model

This paper adopts the average model of the switch mode converters. The formulation of the DER controllers dynamics is below:

$$\frac{\mathrm{d}\boldsymbol{\delta}}{\mathrm{d}t} = \boldsymbol{\omega} - \omega_s \tag{27a}$$

$$\frac{\mathrm{d}\boldsymbol{P}}{\mathrm{d}t} = \boldsymbol{\omega}_c(-\boldsymbol{P} + \boldsymbol{v}_{oD}\boldsymbol{i}_{oD} + \boldsymbol{v}_{oQ}\boldsymbol{i}_{oQ}) \tag{27b}$$

$$\frac{\mathrm{d}\boldsymbol{Q}}{\mathrm{d}t} = \boldsymbol{\omega}_c(-\boldsymbol{Q} + \boldsymbol{v}_{oQ}\boldsymbol{i}_{oD} - \boldsymbol{v}_{oD}\boldsymbol{i}_{oQ}) \tag{27c}$$

$$\frac{\mathrm{d}\boldsymbol{\phi}}{\mathrm{d}t} = \boldsymbol{v}_o^* - \boldsymbol{v}_o - (\boldsymbol{\omega} - \omega_s)\boldsymbol{I}_s\boldsymbol{\phi} \tag{27d}$$

$$\frac{\mathrm{d}\boldsymbol{\gamma}}{\mathrm{d}t} = \boldsymbol{i}_L^* - \boldsymbol{i}_L - (\boldsymbol{\omega} - \omega_s)\boldsymbol{I}_s\boldsymbol{\gamma} \tag{27e}$$

$$\boldsymbol{L}_f\frac{\mathrm{d}\boldsymbol{i}_L}{\mathrm{d}t} = -\boldsymbol{r}_f\boldsymbol{i}_L + \omega_s\boldsymbol{I}_s\boldsymbol{L}_f\boldsymbol{i}_L + (\boldsymbol{v}_i^* - \boldsymbol{v}_o) \tag{27f}$$

$$\boldsymbol{C}_f\frac{\mathrm{d}\boldsymbol{v}_o}{\mathrm{d}t} = \omega_s\boldsymbol{I}_s\boldsymbol{C}_f\boldsymbol{v}_o + (\boldsymbol{i}_L - \boldsymbol{i}_o) \tag{27g}$$

Here, the state variables include $\boldsymbol{\delta}$ (DER angle), $\boldsymbol{P}$ (active power generation), $\boldsymbol{Q}$ (reactive power generation), $\boldsymbol{\phi}$ (output signal of the voltage controller in DQ-axis), $\boldsymbol{\gamma}$ (output signal of the current controller in DQ-axis), $\boldsymbol{i}_L$ (DQ-axis current after the output LC filter) and $\boldsymbol{v}_o$ (DQ-axis voltage of DER). The whole controller is modelled in the DQ-axis (see [30] for detailed structures) and ω_c, r_f, L_f, C_f are controller parameters. Specifically, the angular speed $\boldsymbol{\omega}$ is governed by the droop control in (1) and/or the secondary control in (3).

B. Power Load Model

An arbitrary static power load is formulated as:

$$P_l = P_l(v, i, \omega_s), Q_l = Q_l(v, i, \omega_s) \tag{28}$$

Here, P_l and Q_l respectively denote the active/reactive power load characteristics, which are functions of load voltage v, load current i and system frequency ω_s. The load is connected to the NMs via a brach with the coupling impedance of $r_{lc} + j\omega_s L_{lc}$. This topology is realistic because the coupling impedance, large or small, always exist between a load and the grid.

Denote the DQ-axis voltage and current of the power load as v_{lD}, v_{lQ}, i_{lD} and i_{lQ}. Denote the DQ-axis bus voltage at the connection bus as v_{bD}, v_{bQ}. The active/reactive load power can be computed as follows:

$$P_l = v_{lD}i_{lD} + v_{lQ}i_{lQ}, Q_l = v_{lQ}i_{lD} - v_{lD}i_{lQ} \tag{29}$$

which leads to:

$$\begin{bmatrix} v_{lD} \\ v_{lQ} \end{bmatrix} = \begin{bmatrix} i_{lD} & i_{lQ} \\ -i_{lQ} & i_{lD} \end{bmatrix}^{-1} \begin{bmatrix} P_l \\ Q_l \end{bmatrix} \triangleq \begin{bmatrix} \hat{v}_D(v_{lD}, v_{lQ}, i_{lD}, i_{lQ}, \omega_s) \\ \hat{v}_Q(v_{lD}, v_{lQ}, i_{lD}, i_{lQ}, \omega_s) \end{bmatrix}$$

Consequently, the dynamic of the coupling impedance is formulated as:

$$\begin{aligned} \frac{\mathrm{d}i_{lD}}{\mathrm{d}t} &= -\frac{r_{lc}}{L_{lc}}i_{lD} + \omega_s i_{lQ} + \frac{1}{L_{lc}}(v_{bD} - \hat{v}_D) \\ \frac{\mathrm{d}i_{lQ}}{\mathrm{d}t} &= -\frac{r_{lc}}{L_{lc}}i_{lQ} - \omega_s i_{lD} + \frac{1}{L_{lc}}(v_{bQ} - \hat{v}_Q) \end{aligned} \tag{30}$$

Equation (30) describes the final power load model with an implicit formulation of the load characteristics. It should be taken into the NMs model in replacement of (4) to incorporate a generic power load model. Since (30) is still in the identical form of (8b), the DAE-ODE conversion devised in Section II-C can be readily performed to construct the ODE-enabled NMs model. Further, for the dynamic power loads (such as electromotor), the coupling impedance as well as the internal dynamics of the power loads will together formulate the power load model, which is still coincident with the standard form in (8b) so that the ODE-enabled NMs model readily works.

C. Detailed Expressions of Equation (8)

This Appendix presents the detailed expressions of vectors/matrices/functions in (8).

The state variable vectors of (8) are as follows:

$$\boldsymbol{z} = [\boldsymbol{\delta}; \boldsymbol{P}; \boldsymbol{Q}; \boldsymbol{\phi}; \boldsymbol{\gamma}; \boldsymbol{i}_L; \boldsymbol{v}_o; \boldsymbol{\Omega}; \boldsymbol{e}], \boldsymbol{i} = [\boldsymbol{i}_o; \boldsymbol{i}_l; \boldsymbol{i}_b] \tag{31}$$

where $\boldsymbol{i}$ gathers the DQ-axis current outflow of DERs, power loads and power branches; $\boldsymbol{z}$ gathers the other state variables. Based on the outflow current formulation of each component in (4)-(7), the matrices $\boldsymbol{A}$ and $\boldsymbol{B}$, and the nonlinear function $\boldsymbol{h}$ in (8) are formulated as follows:

$$\boldsymbol{A} = \begin{bmatrix} -\boldsymbol{L}_o^{-1}\boldsymbol{M}_o \\ \boldsymbol{L}_l^{-1}\boldsymbol{M}_l \\ \boldsymbol{L}_b^{-1}\boldsymbol{M}_b \end{bmatrix}, \boldsymbol{B} = \begin{bmatrix} \boldsymbol{M}_o^T & -\boldsymbol{M}_l^T & -\boldsymbol{M}_b^T \end{bmatrix}$$

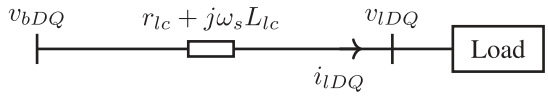

Fig. 20. Illustration of power load model connected to the NMs.

TABLE II
PARAMETERS OF DERS

DER No.	1	2	3	4	5
Loc. node	1	6	13	25	33
Controller parameters [1]	m_p	n_q	r_o (p.u.)	L_o (p.u.)	F
	1.5%	6%	0	6.24×10^{-3}	0.75
	k_{pv}	k_{iv}	k_{pc}	k_{ic}	
	1	1	0.2	2	

[1] m_p: active power droop gain; n_q: reactive power droop gain; r_o: coupling resistance; L_o: coupling inductance; F: current feed-forward gain; k_{pv}: voltage proportional gain; k_{iv}: voltage integral gain; k_{pc}: current proportional gain; k_{ic}: current integral gain;

TABLE III
PARAMETERS OF POWER LOADS

Load No.	Loc. node	r_l (p.u.)	L_l (p.u.)	Load No.	Loc. node	r_l (p.u.)	L_l (p.u.)
1	2	3.32	2.33	15	18	3.68	2.57
2	3	3.67	2.57	16	19	3.69	2.58
3	4	2.75	1.92	17	20	3.66	2.56
4	5	5.49	3.84	18	21	3.66	2.56
5	7	1.64	1.15	19	22	3.65	2.55
6	8	1.64	1.15	20	23	3.66	2.56
7	9	5.50	3.85	21	24	0.78	0.54
8	10	5.52	3.86	22	26	5.48	3.83
9	11	7.38	5.16	23	27	5.47	3.82
10	12	5.54	3.88	24	28	5.42	3.79
11	14	2.74	1.91	25	29	2.70	1.89
12	15	4.89	4.08	26	30	0.24	0.72
13	16	5.55	3.89	27	31	2.17	1.51
14	17	5.53	3.87	28	32	1.55	1.08

$$\boldsymbol{h}(\boldsymbol{i},\boldsymbol{z}) = diag\left(\begin{bmatrix}\boldsymbol{L}_o^{-1}(-\boldsymbol{r}_o+\omega_s\boldsymbol{I}_s\boldsymbol{L}_o)\\ \boldsymbol{L}_l^{-1}(-\boldsymbol{r}_l+\omega_s\boldsymbol{I}_s\boldsymbol{L}_l)\\ \boldsymbol{L}_b^{-1}(-\boldsymbol{r}_b+\omega_s\boldsymbol{I}_s\boldsymbol{L}_b)\end{bmatrix}\right)\boldsymbol{i}+\begin{bmatrix}\boldsymbol{L}_o^{-1}\boldsymbol{v}_o\\ \boldsymbol{0}\\ \boldsymbol{0}\end{bmatrix}$$

where $diag(\cdot)$ denotes the diagonalization function. Then, based on the detailed component models of DERs in (27) and (2)-(3), the nonlinear function $\boldsymbol{g}$ in (8) is formulated in the vector form as:

$$\boldsymbol{g}=\begin{bmatrix}\boldsymbol{\omega}-\omega_s\\ \boldsymbol{\omega}_c(-\boldsymbol{P}+\boldsymbol{v}_{oD}\boldsymbol{i}_{oD}+\boldsymbol{v}_{oQ}\boldsymbol{i}_{oQ})\\ \boldsymbol{\omega}_c(-\boldsymbol{Q}+\boldsymbol{v}_{oQ}\boldsymbol{i}_{oD}-\boldsymbol{v}_{oD}\boldsymbol{i}_{oQ})\\ \boldsymbol{v}_o^*-\boldsymbol{v}_o-(\boldsymbol{\omega}-\omega_s)\boldsymbol{I}_s\boldsymbol{\phi}\\ \boldsymbol{i}_L^*-\boldsymbol{i}_L-(\boldsymbol{\omega}-\omega_s)\boldsymbol{I}_s\boldsymbol{\gamma}\\ \boldsymbol{L}_f^{-1}(-\boldsymbol{r}_f\boldsymbol{i}_L+\omega_s\boldsymbol{I}_s\boldsymbol{L}_f\boldsymbol{i}_L+\boldsymbol{v}_i^*-\boldsymbol{v}_o)\\ \boldsymbol{C}_f^{-1}(\omega_s\boldsymbol{I}_s\boldsymbol{C}_f\boldsymbol{v}_o+\boldsymbol{i}_L-\boldsymbol{i}_o)\\ -\boldsymbol{\alpha}_{l/f}(\boldsymbol{\omega}-\omega^*)-\boldsymbol{A}_{l/f}\boldsymbol{\Omega}-\boldsymbol{C}_{l/f}\boldsymbol{\Omega}_l\\ -\boldsymbol{\beta}_{l/f}(\boldsymbol{E}-\boldsymbol{E}^*)-\boldsymbol{B}_{l/f}(\boldsymbol{Q}\oslash\boldsymbol{Q}_n)-\boldsymbol{D}_{l/f}(\boldsymbol{Q}_l\oslash\boldsymbol{Q}_{n,l})\end{bmatrix}$$

TABLE IV
PARAMETERS OF BRANCHES

Branch No.	From node	To node	Branch No.	From node	To node
1	1	2	17	17	18
2	2	3	18	2	19
3	3	4	19	19	20
4	4	5	20	20	21
5	5	6	21	21	22
6	6	7	22	3	23
7	7	8	23	23	24
8	8	9	24	24	25
9	9	10	25	6	26
10	10	11	26	26	27
11	11	12	27	27	28
12	12	13	28	28	29
13	13	14	29	29	30
14	14	15	30	30	31
15	15	16	31	31	32
16	16	17	32	32	33

[1] Without loss of generality, impedance of each branch are assumed homogeneous with $r_b = 7.79\times10^{-4}$p.u., $L_b = 6.24\times10^{-3}$p.u..

where $\boldsymbol{A}_{l/f}$ refers to $\boldsymbol{A}_l$ or $\boldsymbol{A}_f$ according to whether the DER is a leader or a follower in the secondary control; $\boldsymbol{\alpha}_{l/f}$, $\boldsymbol{\beta}_{l/f}$, $\boldsymbol{B}_{l/f}$, $\boldsymbol{C}_{l/f}$ and $\boldsymbol{D}_{l/f}$ are similarly defined.

APPENDIX B
TEST SYSTEM PARAMETERS

This appendix provides the parameters of the test system in Section IV. The test system is composed of 4 microgrids, as illustrated in Fig. 1.

REFERENCES

[1] Z. Bie, P. Zhang, G. Li, B. Hua, M. Meehan, and X. Wang, "Reliability evaluation of active distribution systems including microgrids," *IEEE Trans. Power Syst.*, vol. 27, no. 4, pp. 2342–2350, Nov. 2012.
[2] M. Eskandari, L. Li, M. H. Moradi, P. Siano, and F. Blaabjerg, "Active power sharing and frequency restoration in an autonomous networked microgrid," *IEEE Trans. Power Syst.*, vol. 34, no. 6, pp. 4706–4717, Nov. 2019.
[3] Z. Wang, B. Chen, J. Wang, M. M. Begovic, and C. Chen, "Coordinated energy management of networked microgrids in distribution systems," *IEEE Trans. Smart Grid*, vol. 6, no. 1, pp. 45–53, Jan. 2014.
[4] N. Soni, S. Doolla, and M. C. Chandorkar, "Improvement of transient response in microgrids using virtual inertia," *IEEE Trans. Power Del.*, vol. 28, no. 3, pp. 1830–1838, Jul. 2013.
[5] S. M. Ashabani and Y. A.-R. I. Mohamed, "A flexible control strategy for grid-connected and islanded microgrids with enhanced stability using nonlinear microgrid stabilizer," *IEEE Trans. Smart Grid*, vol. 3, no. 3, pp. 1291–1301, Sep. 2012.
[6] Y. Han, P. M. Young, A. Jain, and D. Zimmerle, "Robust control for microgrid frequency deviation reduction with attached storage system," *IEEE Trans. Smart Grid*, vol. 6, no. 2, pp. 557–565, Mar. 2015.
[7] S. Dasgupta, S. N. Mohan, S. K. Sahoo, and S. K. Panda, "A plug and play operational approach for implementation of an autonomous-microgrid system," *IEEE Trans. Ind. Informat.*, vol. 8, no. 3, pp. 615–629, Aug. 2012.
[8] R. Majumder, "Some aspects of stability in microgrids," *IEEE Trans. Power Syst.*, vol. 28, no. 3, pp. 3243–3252, Aug. 2013.
[9] P. Kundur, *Power System Stability and Control*. New York, NY, USA: McGraw-Hill, 1994.
[10] M. Farrokhabadi *et al.*, "Microgrid stability definitions, analysis, and examples," *IEEE Trans. Power Syst.*, vol. 35, no. 1, pp. 13–29, Jan. 2020.
[11] P. Hart and B. Lesieutre, "Energy function for a grid-tied, droop-controlled inverter," in *Proc. North Amer. Power Symp.*, 2014, pp. 1–6.

[12] M. Kabalan, P. Singh, and D. Niebur, "Nonlinear Lyapunov stability analysis of seven models of a dc/ac droop controlled inverter connected to an infinite bus," *IEEE Trans. Smart Grid*, vol. 10, no. 1, pp. 772–781, Jan. 2017.
[13] Z. Shuai *et al.*, "Transient angle stability of virtual synchronous generators using Lyapunov's direct method," *IEEE Trans. Smart Grid*, vol. 10, no. 4, pp. 4648–4661, Jul. 2019.
[14] M. Kabalan, P. Singh, and D. Niebur, "Large signal Lyapunov-based stability studies in microgrids: A review," *IEEE Trans. Smart Grid*, vol. 8, no. 5, pp. 2287–2295, Sep. 2017.
[15] X. Wu, "A two-layer distributed cooperative control method for islanded networked microgrid systems," *IEEE Trans. Smart Grid*, vol. 11, no. 2, pp. 942–957, Mar. 2020.
[16] K. P. Schneider *et al.*, "Improving primary frequency response to support networked microgrid operations," *IEEE Trans. Power Syst.*, vol. 34, no. 1, pp. 659–667, Jan. 2019.
[17] Z. Y. Dong, J. H. Zhao, and D. J. Hill, "Numerical simulation for stochastic transient stability assessment," *IEEE Trans. Power Syst.*, vol. 27, no. 4, pp. 1741–1749, Nov. 2012.
[18] Y. Li, P. Zhang, and P. B. Luh, "Formal analysis of networked microgrids dynamics," *IEEE Trans. Power Syst.*, vol. 33, no. 3, pp. 3418–3427, May 2018.
[19] Y. Li, P. Zhang, M. Althoff, and M. Yue, "Distributed formal analysis for power networks with deep integration of distributed energy resources," *IEEE Trans. Power Syst.*, vol. 34, no. 6, pp. 5147–5156, Nov. 2019.
[20] J. W. Simpson-Porco, Q. Shafiee, F. Dörfler, J. C. Vasquez, J. M. Guerrero, and F. Bullo, "Secondary frequency and voltage control of islanded microgrids via distributed averaging," *IEEE Trans. Ind. Electron.*, vol. 62, no. 11, pp. 7025–7038, Nov. 2015.
[21] P. Vorobev, P.-H. Huang, M. Al Hosani, J. L. Kirtley, and K. Turitsyn, "A framework for development of universal rules for microgrids stability and control," in *Proc. 56th IEEE Conf. Decis. Control*, 2017, pp. 5125–5130.
[22] P. Vorobev, P.-H. Huang, M. Al Hosani, J. L. Kirtley, and K. Turitsyn, "High-fidelity model order reduction for microgrids stability assessment," *IEEE Trans. Power Syst.*, vol. 33, no. 1, pp. 874–887, Jan. 2018.
[23] X. Guo, Z. Lu, B. Wang, X. Sun, L. Wang, and J. M. Guerrero, "Dynamic phasors-based modeling and stability analysis of droop-controlled inverters for microgrid applications," *IEEE Trans. Smart Grid*, vol. 5, no. 6, pp. 2980–2987, Nov. 2014.
[24] H. D. Nguyen, "Robust stability assessment for future power systems," Ph.D. dissertation, Dept. Mech. Eng., Massachusetts Inst. Technol., Massachusetts, MA, USA, 2018.
[25] M. Althoff and B. H. Krogh, "Zonotope bundles for the efficient computation of reachable sets," in *Proc. 50th IEEE Conf. Decis. Control*, 2011, pp. 6814–6821.
[26] M. Berz and G. Hoffstätter, "Computation and application of Taylor polynomials with interval remainder bounds," *Reliable Comput.*, vol. 4, no. 1, pp. 83–97, 1998.
[27] M. Althoff, O. Stursberg, and M. Buss, "Reachability analysis of linear systems with uncertain parameters and inputs," in *Proc. 46th IEEE Conf. Decis. Control*, 2007, pp. 726–732.
[28] M. Liou, "A novel method of evaluating transient response," *Proc. IEEE*, vol. 54, no. 1, pp. 20–23, 1966.
[29] M. Althoff, O. Stursberg, and M. Buss, "Reachability analysis of nonlinear systems with uncertain parameters using conservative linearization," in *Proc. 47th IEEE Conf. Decis. Control*, 2008, pp. 4042–4048.
[30] N. Pogaku, M. Prodanovic, and T. C. Green, "Modeling, analysis and testing of autonomous operation of an inverter-based microgrid," *IEEE Trans. Power Electron.*, vol. 22, no. 2, pp. 613–625, Mar. 2007.
[31] H. W. Dommel, *EMTP Theory Book*. Vancouver, Canada: Microtran Power System Analysis Corporation, 1996.
[32] D. Coppersmith and S. Winograd, "Matrix multiplication via arithmetic progressions," in *Proc. 19th Annu. ACM Symp. Theory Comput.*, 1987, pp. 1–6.
[33] B. Bicsi, *Network Design Basics for Cabling Professionals*. New York, NY, USA: McGraw-Hill Professional, 2002.

Yifan Zhou (Member, IEEE) received the B.S. and Ph.D. degrees from Tsinghua University, Beijing, China, in 2014 and 2019, respectively, both in electrical engineering. She is currently a Postdoctoral Researcher with Stony Brook University, Stony Brook, NY, USA. Her research interests include microgrid stability and control, formal methods and reachability analysis, and quantum computing.

Peng Zhang (Senior Member, IEEE) received the Ph.D. degree in electrical engineering from the University of British Columbia, Vancouver, BC, Canada, in 2009. He is a SUNY Empire Innovation Professor with Stony Brook University, New York. He has a Joint Appointment with Brookhaven National Laboratory as a Staff Scientist. Previously, he was a Centennial Associate Professor and a Francis L. Castleman Associate Professor with the University of Connecticut, Storrs, CT, USA. During 2006–2010, he was a System Planning Engineer with BC Hydro and Power Authority, Canada. His research interests include programmable microgrids, networked microgrids, quantum security, quantum computing, power system stability and control, cyber security, formal methods and reachability analysis, and software-defined networking.

He is an individual member of CIGRÉ. He is an Editor for the IEEE TRANSACTIONS ON POWER SYSTEMS, the IEEE TRANSACTIONS ON SUSTAINABLE ENERGY and the IEEE POWER AND ENERGY SOCIETY LETTERS, and an Associate Editor for the IEEE JOURNAL OF OCEANIC ENGINEERING.

Meng Yue (Member, IEEE) received the B.S. degree in electrical engineering from Xi'an Technological University, Xi'an, China, in 1990, the M.S. degree in electrical engineering from Tianjin University, Tianjin, China, in 1995, and the Ph.D. degree in electrical engineering from Michigan State University, East Lansing, MI, USA, in 2002.

He is currently with the Department of Sustainable Energy Technologies, Brookhaven National Laboratory, Upton, NY, USA. His research interests include power system stability and dynamic performance analysis, preventive, corrective, and stabilizing control, renewable energy modeling and integration, and high performance computing and probabilistic risk assessment applications in power systems.